The Cryosphere, 10, 2057–2068, 2016
www.the-cryosphere.net/10/2057/2016/
doi:10.5194/tc-10-2057-2016

The Cryosphere Open Access EGU

Direct visualization of solute locations in laboratory ice samples

Ted Hullar and Cort Anastasio

Department of Land, Air, and Water Resources, University of California, Davis, USA

Correspondence to: Cort Anastasio (canastasio@ucdavis.edu)

Received: 29 October 2015 – Published in The Cryosphere Discuss.: 15 January 2016
Revised: 5 July 2016 – Accepted: 2 August 2016 – Published: 14 September 2016

Abstract. Many important chemical reactions occur in polar snow, where solutes may be present in several reservoirs, including at the air–ice interface and in liquid-like regions within the ice matrix. Some recent laboratory studies suggest chemical reaction rates may differ in these two reservoirs. While investigations have examined where solutes are found in natural snow and ice, few studies have examined either solute locations in laboratory samples or the possible factors controlling solute segregation. To address this, we used micro-computed tomography (microCT) to examine solute locations in ice samples prepared from either aqueous cesium chloride (CsCl) or rose bengal solutions that were frozen using several different methods. Samples frozen in a laboratory freezer had the largest liquid-like inclusions and air bubbles, while samples frozen in a custom freeze chamber had somewhat smaller air bubbles and inclusions; in contrast, samples frozen in liquid nitrogen showed much smaller concentrated inclusions and air bubbles, only slightly larger than the resolution limit of our images ($\sim 2\,\mu m$). Freezing solutions in plastic vs. glass vials had significant impacts on the sample structure, perhaps because the poor heat conductivity of plastic vials changes how heat is removed from the sample as it cools. Similarly, the choice of solute had a significant impact on sample structure, with rose bengal solutions yielding smaller inclusions and air bubbles compared to CsCl solutions frozen using the same method. Additional experiments using higher-resolution imaging of an ice sample show that CsCl moves in a thermal gradient, supporting the idea that the solutes in ice are present in mobile liquid-like regions. Our work shows that the structure of laboratory ice samples, including the location of solutes, is sensitive to the freezing method, sample container, and solute characteristics, requiring careful experimental design and interpretation of results.

1 Introduction

Snowpacks can be important locations for a variety of chemical reactions, particularly in polar regions (Bartels-Rausch et al., 2014; Domine and Shepson, 2002). Because light can penetrate several tens of centimeters into the snowpack, photochemical reactions are particularly important (Grannas et al., 2007), including nitrate photolysis forming NO_x (Beine et al., 2002; Chu and Anastasio, 2003; Jacobi et al., 2004), hydrogen peroxide photolysis forming hydroxyl radical (Chu and Anastasio, 2005; Jacobi et al., 2006), and transformation of organics (Dibb and Arsenault, 2002; Sumner and Shepson, 1999).

A variety of potential chemical reactants have been identified in snowpacks; concentrations can vary considerably, with typical concentrations on the order of 10 µM in clean Arctic snows (Yang et al., 1996). Impurities can integrate into snow crystals during formation, or be deposited onto the surface of formed crystals. Reactants and products also partition between the snow crystals and the overlying air; the large surface area of the snow crystals provides an extensive environment for reactions to occur. As the snowpack consolidates and snow grains metamorphose, chemical compounds can remain at the surface of the crystals or become trapped internally at grain boundaries or triple junctions (Bartels-Rausch et al., 2014; Domine et al., 2008; Grannas et al., 2007).

There appear to be three reservoirs for impurities in snow: a quasi-liquid layer (QLL) at the ice–air interface; liquid-like regions (LLRs) within the ice (e.g., at grain boundaries); and in the bulk ice matrix, i.e., between frozen water molecules (Barret et al., 2011; Grannas et al., 2007; Jacobi et al., 2004). While the exact location of solutes in snow is not well understood (Bartels-Rausch et al., 2014), the location is important for several reasons. First, chemicals in a surface QLL can be more readily released to the atmosphere compared to impuri-

ties segregated into an internal LLR; furthermore, gas-phase oxidants and other species can readily partition from the air onto solutes at the air–ice interface. Second, photon fluxes can vary considerably in various locations within the snowpack (Phillips and Simpson, 2005), although there appear to be only small differences within crystals themselves (McFall and Anastasio, 2016). Third, the rates of reactions of impurities appear to vary with location. For example, photolysis rates of PAHs (polycyclic aromatic hydrocarbons) have been reported to be up to 5 times faster in surface QLLs compared to in whole ice samples (where PAHs are likely in LLRs) or in aqueous solution (Kahan and Donaldson, 2007, 2010; Ram and Anastasio, 2009). An investigation of reactions in frozen solutions (Kurkova et al., 2011) suggested the QLL and LLR physical reaction environments are substantially different, with QLLs best represented by a 2-D cage and LLRs by a 3-D cage. This work also found that the cage effect (i.e., the tendency for a compound to be surrounded by solvent molecules, which can impede the ability of a compound to react) at a given temperature was much more pronounced for reactions occurring in QLLs than LLRs, with solutes in QLLs having less mobility compared to solutes in LLRs.

Because of the potential reactivity differences between the reservoirs, understanding reaction rates in different reservoirs requires knowing where solutes are located. Solute locations in natural snow and ice samples have been studied using electron microscopy (Barnes et al., 2003; Lomonaco et al., 2009; Rosenthal et al., 2007) and were found to preferentially segregate to grain boundaries and triple junctions. Additional work has evaluated the nature of these compartments, showing that solutes segregate and concentrate in LLRs (Heger et al., 2005, 2006). When an aqueous solution is frozen, most solutes are excluded from the forming ice matrix (Hobbs, 1974; Petrenko and Whitworth, 1999), often forming platelets of ice separated by brine or dendritic structures (Rohatgi and Adams, 1967; Shumskii, 1964). Recently, some studies have used various techniques to directly examine the location of solutes themselves in laboratory snow and ice samples (Cheng et al., 2010; Miedaner, 2007; Miedaner et al., 2007). Nonetheless, solute location is poorly understood in many experimental systems and is most often inferred from the way the sample is made (Kahan et al., 2010) or from chemical behavior (Kurkova et al., 2011).

The main goal of this paper is to examine the location of solutes in laboratory-prepared frozen solutions. In order to do this, we use X-ray computed tomography (CT), a technique that has been used to create three-dimensional images of a variety of biological and natural materials (Blanke et al., 2013; Evans et al., 2008). High-resolution micro-computed tomography (microCT), which is capable of a spatial resolution of $< 10\,\mu m$, has been used to look at the structure of natural snow and ice (Chen and Baker, 2010; Heggli et al., 2011; Lomonaco et al., 2011; Obbard et al., 2009). But to our knowledge this method has not been used to investigate the structure and solute locations for laboratory samples prepared under reproducible conditions with specific solutes.

Thus here we examine the locations of impurities in frozen aqueous solutions prepared in the laboratory. We are primarily interested in the locations of solutes in ices prepared using different freezing methods aimed at putting solutes in specific reservoirs within the ice; these methods, or similar ones, have been used both in our previous research and by other investigators. In this work we focus on cesium chloride (CsCl) as our solute. However, because previous studies (Cheng et al., 2010; Rohatgi and Adams, 1967) have found that different solutes can affect freezing morphology and therefore may influence solute location, we also imaged ice containing the organic compound rose bengal (4,5,6,7-tetrachloro-2′,4′,5′,7′-tetraiodofluorescein). For our samples we present both qualitative (visual) and semi-quantitative (tabular and graphical) results.

2 Methods

We prepared samples by freezing 1.0 mM aqueous solutions of cesium chloride or, in a few cases, 1.0 mM rose bengal. High-purity water ("Milli-Q water") was produced from house-treated deionized water that was run through a Barnstead International DO813 activated carbon cartridge and then a Millipore Milli-Q Plus system. We chose cesium chloride (Sigma-Aldrich, 99.9 %) for our primary solute because of its high solubility in water and high X-ray mass attenuation coefficient ($\sim 4.4\,cm^2\,g^{-1}$ at 70 keV; NIST, 2015), enabling visualization of low concentrations in our microCT system. We also used rose bengal to study the impacts of solute size and polarity on sample morphology. While 1.0 mM of solute is higher than typical total solute concentrations in continental (inland) natural snows, it is within the range of concentrations measured in coastal snowpacks (Beine et al., 2011; Douglas and Sturm, 2004; Yang et al., 1996). The chosen concentration allows easy visualization in our system and provides enough material to evaluate spatial patterns in the sample.

We froze most samples as a 500 µL aliquot in a capped glass vial (approximately 3 cm high and 1 cm in diameter, 0.8 mm wall thickness, with a total vial volume of ~ 2 mL) using one of three methods. These methods were chosen because they had been used in our laboratory, as well as others, and also due to differences in the speed of heat removal from the samples; we discuss later the expected morphologies for the various sample types. In the first technique ("freezer"), we placed samples upright on a plastic plate in a laboratory freezer at approximately $-20\,°C$; freezing took approximately 1 h. In the second technique ("freeze chamber"), we froze samples upright in a custom-built freeze chamber (Hullar and Anastasio, 2011) whose base was cooled to either -10 or $-20\,°C$. Typically, the sample sat directly on the base of the freeze chamber surrounded by air. However, we

also froze some samples surrounded by drilled metal plates, effectively placing the sample in a metal "well"; the distance between the sample and the surrounding plates was around 1 mm. In the third technique ("liquid nitrogen" or "LN2") we froze samples by putting the aqueous sample in a vial, capping it, and then immersing it in a bath of liquid nitrogen deeper than the height of the liquid in the vial; freezing time was ~ 30 s. We allowed all samples to anneal at $-10\,^{\circ}$C for at least 1 h before imaging. We froze a small number of samples either in polypropylene vials (wall thickness ~ 1 mm) or with a larger sample volume (750 µL).

We imaged samples using a MicroXCT-200 (Zeiss Instruments) microCT scanner. To maintain our samples at $-10\,^{\circ}$C, samples were held in a custom cold stage for the MicroXCT-200 (Hullar et al., 2014). The custom cold stage was placed on the scanner's sample stage, whose position is controlled by the scanner software to submicron precision. Scanning parameters were set based on the manufacturer's guidelines. For most imaging, we set source and detector distances to 40 and 130 mm, respectively; voltage and power were set at 70 keV and 7.9 W, and the manufacturer's LE3 custom filter was used for beam filtration. The microCT acquired 1600 projections over 360° of rotation, with an exposure time of 2 s. Images were reconstructed using the manufacturer's software on an isotropic voxel grid with 15.9358 µm edge lengths. Some samples were analyzed at higher resolution, with a voxel edge length of 2.1146 µm. For these samples, we set source and detector distances to 60 and 18 mm; used the LE5 beam filter; collected 2400 projections spanning 360°; and set beam voltage, power, and exposure time to 60 keV, 6 W, and 30 s, respectively. The microCT scanner software outputs slicewise TIFF images of the x–y plane of the sample, with grayscale values corresponding to the radiodensity of each voxel at that z plane.

We imported digital TIFF images into the Amira software package (Visualization Sciences Group, FEI) for reconstruction and segmentation. Our segmentation procedure used the Amira segmentation tools to isolate the sample from surrounding materials; generally, our procedure should include very little sample container at the expense of excluding some small amounts of sample in contact with the vial wall. Similarly, the segmentation procedure excludes very little sample in contact with air above the sample, while including small amounts of top air as a sample. Some images presented here were mathematically smoothed by the software, which sometimes resulted in small features (< 80 µm in diameter) being eliminated from movies and still images; however, smoothing did not substantially change the interpretation of our results. In some cases we prepared histograms of the data, which were not smoothed and include all sample data.

To quantitate CsCl concentration in each voxel, we first imaged samples of Milli-Q water, as both liquid and ice, and measured the average radiodensity (image grayscale value) of a subvolume within each sample. As expected, the average radiodensity of ice (4948 ± 160 (1σ)) was less than that of liquid water (5372 ± 194 (1σ)) due to the lower density of ice. Our measured radiodensity ratio between ice (at $-10\,^{\circ}$C) and water (at $20\,^{\circ}$C) was 0.921, matching a calculated density ratio from literature values (Haynes, 2014) of 0.921. Next, we imaged eight aqueous solutions of CsCl at varying concentrations (1.0 mM to 5.0 M) to construct a calibration curve. Plotting these points (Fig. 1) shows a linear relationship between CsCl concentration and measured radiodensity, with a y-intercept value within the range of our measured radiodensities for pure liquid water. Therefore, the measured radiodensity of a voxel within a sample containing CsCl in solution (or ice) is linearly related to the amount of CsCl present in the voxel. We assume the relationship between CsCl concentration and radiodensity is the same for ice and water. This allows us to determine the amount of CsCl present in a sample voxel by subtracting the average grayscale value of pure water (or ice) and then using the standard curve to calculate the CsCl mass.

When aqueous solutions are frozen, solutes are generally excluded from the forming ice matrix, resulting in two distinct components: pure (or nearly pure) water ice, and a concentrated solution of solute (Cho et al., 2002; Lake and Lewis, 1970; Wettlaufer et al., 1997), which can be present at the air–ice interface (i.e., as a QLL) and/or in LLRs within the sample. Freezing-point depression dictates that the solute concentration in these regions is solely a function of the ice temperature (Cho et al., 2002) and is independent of the solute concentration in the initial solution. For example, at $-10\,^{\circ}$C, the predicted total solute concentration in LLRs is 5.4 M of solute ions, or 2.7 M of a binary salt such as CsCl. This LLR concentration is considerably lower than the solubility limit of CsCl (11.1 M at $20\,^{\circ}$C, 9.6 M at $0\,^{\circ}$C; NIH, 2015) but higher than the solubility limit of rose bengal (1 mM, temperature not given; Neckers, 1989). Therefore, we do not expect CsCl to precipitate, although rose bengal might.

As described earlier, we use the Fig. 1 calibration curve to convert microCT grayscale values of radiodensity for each voxel to the mass of solute in each voxel. While this mass could be expressed as an equivalent concentration in the voxel, we believe it is more accurate to consider each voxel as a mixture of pure water ice (with zero solute) and LLRs (regions with a total solute ion concentration of 5.4 M at $-10\,^{\circ}$C, equivalent to a CsCl concentration of 2.7 M). Thus we express the composition of each voxel as the fraction of voxel volume occupied by liquid-like regions, $V_{\mathrm{LLR}}/V_{\mathrm{VOXEL}}$:

$$\frac{V_{\mathrm{LLR}}}{V_{\mathrm{VOXEL}}} = \frac{(\mathrm{RD_{MEAS}} - \mathrm{RD_{ICE}})/\mathrm{Slope}}{2.7\,\mathrm{M}}, \quad (1)$$

where V_{LLR} is the LLR volume, V_{VOXEL} represents the volume of the entire voxel, $\mathrm{RD_{MEAS}}$ is the measured radiodensity of the voxel, $\mathrm{RD_{ICE}}$ is the radiodensity of pure ice (4948), and Slope is the measured slope of the standard curve line ($10\,409\,\mathrm{M}^{-1}$; Fig. 1). A voxel containing only

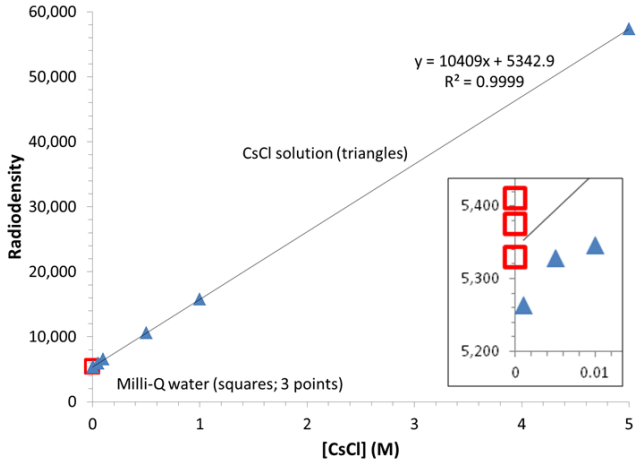

Figure 1. Radiodensity of pure water (red open squares, three data points) and of aqueous solutions containing CsCl (blue triangles).

pure ice has $V_{LLR}/V_{VOXEL} = 0$, while a voxel composed entirely of 5.4 M total solute in water has $V_{LLR}/V_{VOXEL} = 1$. Our estimated concentration of total solute ion concentration in LLRs is based on theoretical calculations and assumes ideal behavior from the solution (Cho et al., 2002; Pruppacher and Klett, 2010). However, at higher concentrations, solutions can deviate from ideal behavior. Pruppacher and Klett (2010) and Haynes (2014) both present data for the freezing-point depression of CsCl, but only up to a salt concentration of 1.8 M (Pruppacher and Klett, 2010) or 1.4 M (Haynes, 2014). Extrapolating their data to the concentrations expected in our samples (i.e., at −10 °C) suggests the CsCl concentration in LLRs would be somewhere between 3 and 3.2 M, i.e., 10–20 % higher than our ideal case concentration, but neither source presents freezing-point depression data measured at such a high concentration. In the absence of measured information for the actual composition of CsCl solutions under our experimental conditions, we have elected to stay with the theoretical prediction of salt concentration of 2.7 M. If the actual LLR solute concentration is higher (lower) than 2.7 M, the V_{LLR}/V_{VOXEL} values presented here would be lower (higher); we estimate the largest magnitude of this error as approximately 20 %. For clarity, we use the measured V_{LLR}/V_{VOXEL} values to segment many of our images into four domains: voxels containing only air (defined as $V_{LLR}/V_{VOXEL} < -3.4$ %), voxels containing ice and little or no solute ($V_{LLR}/V_{VOXEL} = -3.4$ to 2 %), voxels containing a moderate amount of solute ($V_{LLR}/V_{VOXEL} = 2$–10 %), and voxels containing a substantial amount of solute ($V_{LLR}/V_{VOXEL} > 10$ %). We define an "air" voxel as having a radiodensity less than or equal to the average radiodensity of an imaged air sample, i.e., 3996. As noted above, grayscale values from images of pure materials vary somewhat, meaning a clear distinction between two materials with similar average grayscale values is not possible. We chose to set the cutoff for segmenting LLRs at a grayscale value of 5507, a threshold 3 standard deviations greater than the average grayscale value for pure ice, which will essentially eliminate the problem of identifying water ice as solute. However, because of this high threshold it is quite likely that solute is present in some voxels characterized as "ice". On the other hand, voxels defined as having an LLR percentage of 2 % or greater almost certainly contain solute. For CsCl-containing samples, we calculated the mass of CsCl present in each domain. Because the statistical distributions of voxels containing only pure water ice and those containing < 2 % LLR as well as pure water ice overlapped, we could not determine the mass of CsCl present in the ice domain directly. Therefore, we assumed any mass not present in either the LLR 2−10 % or LLR > 10 % domains is present in the ice domain.

3 Results and discussion

We first present imaging results for samples prepared without added solute (frozen Milli-Q water). Figure 2a shows a reconstructed image of a "pure" ice sample prepared by freezing air-saturated Milli-Q in a glass vial in a laboratory freezer; the full movie, which shows the sample rotating, is in Supplement Fig. S1. Air bubbles are visible as light-gray spheroids and are generally located towards the center of the sample, away from the vial walls and base. This is likely because the entire outer surface of the vial was cooled and the water apparently froze from the outside inward. Supporting this idea, some of the bubbles appear to elongate along the radial axes of the sample, similar to the bubble elongation seen by Carte (1961) in a temperature gradient. The isolation of bubbles within the middle of the sample seems to follow Shumskii's (1964) model of the formation of the "central nucleus", with impurities (in this case, air bubbles) forced to the center of a freezing water mass.

Figure 2b shows a reconstruction of a similar Milli-Q sample, but now in which the solution was degassed with helium for 30 min before freezing; the full movie is in Supplement Fig. S2. Because He degassing replaces the more soluble nitrogen and oxygen in the air-saturated solution with less soluble helium, fewer bubbles are present in Fig. 2b. The size of the bubbles, however, is roughly similar in the two figures (approximately 150–300 µm), suggesting bubble size is a function of the freezing method, not of the gas itself.

Figure 2c shows a histogram of the number of voxels containing various radiodensities, represented here as the ratio V_{LLR}/V_{VOXEL}, in the two water ice samples. A ratio of 0 represents the average radiometric density for pure water ice, with values slightly greater or less than 0 indicating noise in the sample images and reconstruction. Voxels containing only air comprise the smaller second peak centered at approximately $V_{LLR}/V_{VOXEL} = -0.05$, which overlaps with the primary (pure ice) peak. Taking into account that the y axis (voxel count) is a log scale, the two curves

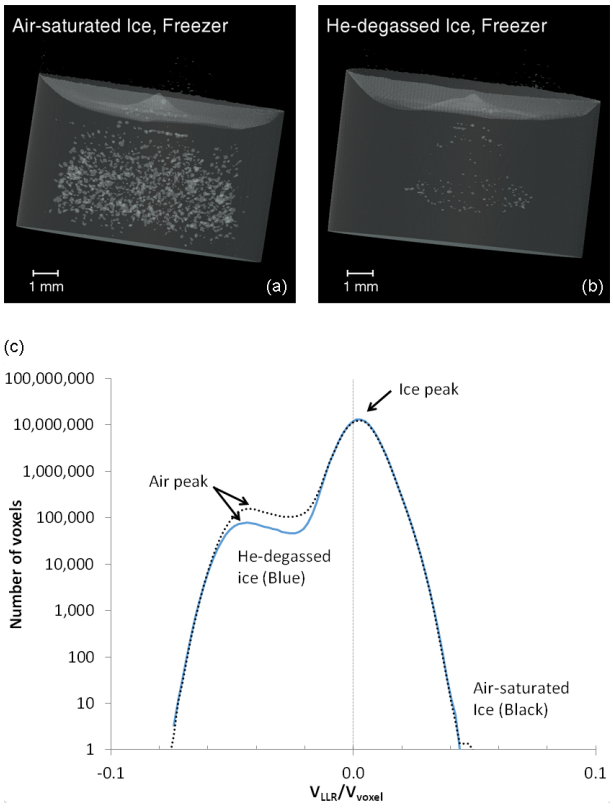

Figure 2. Reconstructed images **(a, b)** and histogram **(c)** of water ice samples frozen in a laboratory freezer, imaged using microCT (∼ 16 µm voxel size) and segmented to show air bubbles (light gray) and the bulk ice matrix (darker gray). The glass sample vial is not shown. The ice in panel **(a)** was made using air-saturated water, while that in panel **(b)** was made with water degassed with helium for 30 min before freezing. Panel **(c)** shows the distributions of the radiodensities within the two samples, expressed as the fraction of each voxel that would be occupied by a liquid-like region (LLR) assuming the total solute concentration is determined by freezing-point depression (i.e., 5.4 M at −10 °C; Cho et al., 2002).

show the volume of gas bubbles is clearly less for the helium-degassed treatment. Table 1 shows the estimated volumes of water ice and gas bubbles in the two samples, as determined by our segmentation process (see Sect. 2). The gas volume in ice made from air-saturated water is approximately 1.4 %, while the ice made from helium-saturated Milli-Q has approximately half the gas volume. Figure 2a and b appear to show a larger difference in gas volume between the two samples, suggesting that many of the small bubbles in the sample imaged in Fig. 2b may have been smoothed away and thus are not visible. For a solution in equilibrium with air at 25 °C, the mole fraction solubility of air (assuming a composition of 20 % oxygen and 80 % nitrogen) is 1.4×10^{-5}, while the value for helium is 7.0×10^{-6} (Haynes, 2014), i.e., half the concentration of air in the solution. The expected volume of bubbles in the helium-degassed treatment agrees well with the observed volume.

Table 1. Sample volumes and fractions by material type.

Sample	Initial solution volume (µL)	Total CsCl mass (µg)	Volume (mm^3)[a]				Volume fraction[a, b]				CsCl mass fraction[a, c]		
			Gas	Water ice	LLR 2–10 %	LLR > 10 %	Gas	Water ice	LLR 2–10 %	LLR > 10 %	Water ice	LLR 2–10 %	LLR > 10 %
MilliQ water													
Freezer	500	0	5.96	430	0	0	0.014	0.986	0	0	–	–	–
Freezer, degassed	500	0	3.23	432	0	0	0.007	0.993	0	0	–	–	–
1 mM CsCl													
Freezer	750	126.3	5.07	716	2.35	0.141	0.007	0.990	0.003	0.00019	0.651	0.233	0.116
Freeze chamber	500	84.2	5.55	473	2.67	0.0176	0.012	0.983	0.006	0.000037	0.640	0.346	0.014
Liquid nitrogen	750	126.3	0	725	1.50	0	0	0.998	0.002	0	0.879	0.121	0.000

[a] "Gas" is defined as having a grayscale value of < 3996, "Water ice" is defined as containing < 2 % liquid-like region (LLR), "LLR 2–10 %" is water ice containing an LLR fraction of between 2 and 10 %, and "LLR > 10 %" is water ice containing > 10 % LLR. The original sample volume (either 500 or 750 µL) is not fully captured in the volumes reported here. The segmentation process eliminates some of the lower part of the sample, reducing the reported volume somewhat.
[b] Fraction of imaged sample volume (not initial solution volume). See text for details.
[c] Fraction of total CsCl mass present in each domain. Because the mass of CsCl present in the water ice compartment could not be determined directly, we assumed any mass not present in either the LLR 2–10 % or LLR > 10 % domain is present in the water ice domain.

Next, we examined the effect of the freezing method on both freezing morphology and solute location. The freezer, freeze chamber, and LN2 sample preparation methods are described in the Methods section. Figure 3 shows the results of imaging several combinations of the freezing method and solute. We start with an image of the ice made by freezing 1.0 mM CsCl in a laboratory freezer. As shown in Fig. 3a (and the Supplement Fig. S3 movie), both air bubbles and concentrated CsCl LLRs are relatively large, with the LLRs tending to wrap around the air bubbles. Figure 3b is a magnification of the red-bordered area in Fig. 3a, showing examples of large solute inclusions wrapped around air bubbles (lighter gray spheroids).

Figure 3c (movie: Supplement Fig. S4) shows a similarly prepared sample to the freezer sample in Fig. 3a, but frozen in our freeze chamber. Compared to the freezer sample, the freeze chamber sample has smaller air bubbles and inclusions, it has more solute present near the top of the sample, and the areas of concentrated solutes (LLRs) are less likely to be associated with the air bubbles. These points are clearly shown in Fig. 3d, which is a magnification of the red-bordered area of Fig. 3c. Considering that these two samples were frozen at similar temperatures, the morphologies are substantially different. As seen in Table 1, the fraction of voxels containing a LLR fraction $>10\,\%$ is about fivefold less in the freeze chamber sample than the freezer sample, while the fraction of voxels with an LLR concentration between 2 and 10 % doubles. This finding indicates the freezing process in the freeze chamber creates smaller LLR inclusions than does the freezer, with LLRs distributed more widely throughout the sample. Additionally, substantial amounts of solute were segregated towards the surface of the freeze chamber sample; presumably, the sample froze from the bottom and solutes were preferentially excluded from the advancing freezing front. However, the same process did not affect the air bubbles, which are well distributed throughout the sample. We believe these structural differences may be due to faster freezing in the freeze chamber sample, as the freeze chamber removes heat more quickly than the freezer because of direct contact between the bottom of the vial and the chilled base plate in the chamber. Previous work (Hallett, 1964; Rohatgi and Adams, 1967) has shown that faster freezing gives closer spacing of ice dendrites or plates in the sample as it freezes, which then leads to smaller solute inclusions or bubbles, similar to our finding here. Supplement Fig. S5 shows a sample prepared in the same way as in Fig. 3c albeit with the metal plates in place in the freeze chamber, which surrounds the vial with metal rather than air. Here, we see similar bubble size and location to those in the sample frozen in the freeze chamber without the metal plates. However, unlike the sample frozen without plates in the freeze chamber, the solute distribution with plates shows no segregation towards the top of the sample, probably because the close proximity of the conductive metal plates removed heat from the

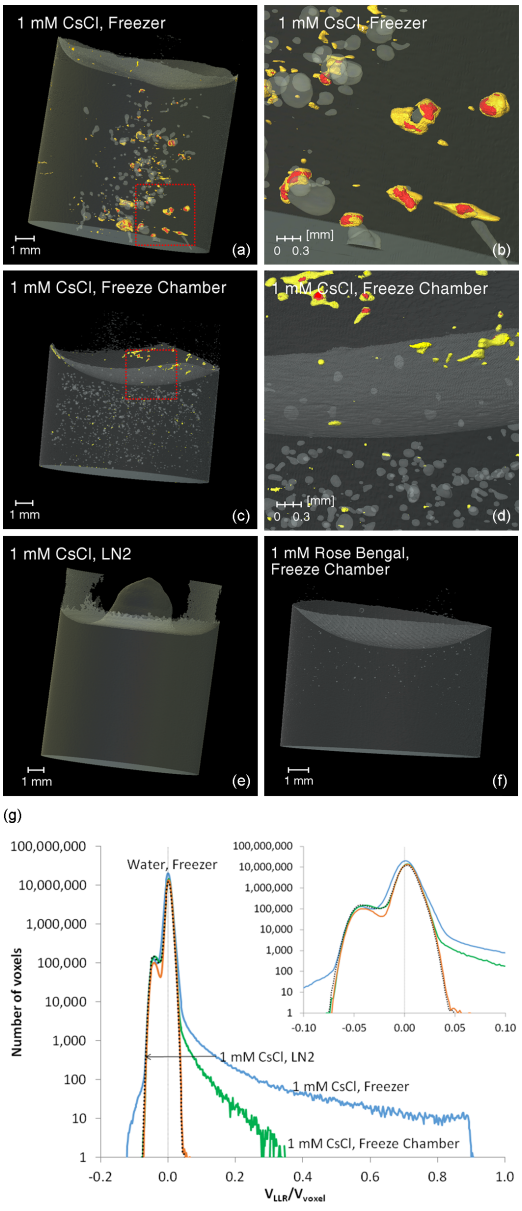

Figure 3. Reconstructed images and histograms of ice samples frozen using three freezing methods and with two different solutes. Samples were imaged using a $\sim 16\,\mu$m voxel size and segmented to show air bubbles (light gray), the bulk ice matrix (darker gray), voxels where V_{LLR}/V_{VOXEL} is between 2 and 10 % (orange), and voxels where $V_{LLR}/V_{VOXEL} > 10\,\%$ (red). The sample vial is not shown. **(a)** 1.0 mM CsCl solution frozen in freezer. **(b)** Magnification of the area in panel **(a)** identified by the dashed red square. **(c)** 1.0 mM CsCl solution frozen in freeze chamber (without metal plates). **(d)** Magnification of the dashed-line area of panel **(c)**. **(e)** 1.0 mM CsCl solution frozen in liquid nitrogen. No air bubbles or inclusions are visible at this scale. **(f)** 1.0 mM rose bengal solution frozen in freeze chamber. **(g)** Histogram showing distribution of voxel counts for the CsCl and Milli-Q water ice samples shown above: water ice frozen in freezer, black dotted line; 1.0 mM CsCl frozen in LN2, orange line; 1.0 mM CsCl frozen in freezer, blue line; 1.0 mM CsCl, frozen in freeze chamber, green line. The inset shows an expanded view from $V_{LLR}/V_{VOXEL} = -0.1$ to 0.1.

sides and bottom of the sample simultaneously, similar to the freezer case.

Results for a 1.0 mM CsCl sample prepared with the third freezing method – liquid nitrogen – are shown in Fig. 3e, with the full movie in Supplement Fig. S6. No air bubbles or significant solute inclusions are visible. However, as discussed earlier, some very small inclusions and air bubbles can be removed by the mathematical smoothing done by the reconstruction software, so very small features ($< \sim 80\,\mu m$) may be present in the sample but lost in the reconstruction. A histogram of raw (i.e., not smoothed) grayscale values from the LN2 sample image does show some voxels contain concentrated solutes (Fig. 3g), as indicated by V_{LLR}/V_{VOXEL} for some voxels towards the right-hand side of the graph being greater than that of pure water ice. As a further test of the possibility of solute inclusions in LN2 samples, we examined unreconstructed cross sections of a 1.0 mM CsCl sample frozen in liquid nitrogen and imaged at $\sim 2\,\mu m$ voxel resolution. As illustrated in Supplement Fig. S7, there are some light (concentrated solute) and dark (air bubble) areas, suggesting some segregation of CsCl and air occurs even with rapid freezing (~ 30 s). However, this effect is less noticeable in the quickly frozen liquid nitrogen sample (Supplement Fig. S7) and much more pronounced in the other two freezing methods (Fig. 3a and c). Analogous findings, although using a very different experimental system, were reported by Heger et al. (2005), who found solutes were concentrated by as many as 6 orders of magnitude with slow (several minutes) freezing but only 3 orders of magnitude when frozen in liquid nitrogen.

Figure 3g shows the histogram for the 1.0 mM CsCl solutions frozen using each of the three freezing methods, as well as for Milli-Q water ice frozen in a laboratory freezer. Unlike the images seen in Fig. 3a through f, where mathematical smoothing can eliminate small structures, the histograms include all the voxels in the sample. As discussed in Fig. 2c, water ice has two overlapping peaks, corresponding to air bubbles (left peak) and ice (right peak). Some voxels, shown in the "saddle" between the two peaks, contain both air bubbles and pure water ice and will therefore have a grayscale value between air and ice. The Fig. 3g histogram clearly shows how CsCl tends to be present in larger LLR volumes in the freezer sample, including some voxels that are almost completely composed of 2.7 M CsCl solution, with a maximum V_{LLR}/V_{VOXEL} of 0.9. This finding supports the idea of solutes segregating to concentrated LLRs during freezing, since if solutes were precipitating and forming solid inclusions in the bulk ice, the calculated ratio in a voxel could be higher than 1. The fact that the ratio gets close to, but never exceeds, 1 is consistent with our tricomponent model of air, relatively pure ice, and concentrated LLRs with a maximum concentration of 5.4 M total solute.

The increased number of air voxels on the left end of the curve for the 1.0 mM CsCl freezer sample represents voxels composed entirely of air. This number is larger than in the water sample, supporting the imaging findings that the presence of solute actually increases the size of air bubbles. For the freeze chamber and LN2 samples, the number of voxels containing only air is smaller, and voxels containing air are more likely to contain at least some fraction of ice or solute. For the freeze chamber sample, the histogram correlates with the images (Fig. 3c and d), with fewer voxels containing a large volume fraction of highly concentrated regions than in the freezer sample. Finally, the liquid nitrogen histogram is nearly identical to water ice, although a few voxels with concentrated solute are present (also seen in Supplement Fig. S7). Next, we examined the impact of solute on freezing morphology and solute location, by replacing CsCl with rose bengal, a large, organic molecule (see structure in Supplement Fig. S8). Figure 3f (movie: Supplement Fig. S9) shows a sample containing 1.0 mM rose bengal frozen in our freeze chamber. Using 1.0 mM rose bengal instead of 1.0 mM CsCl (Fig. 3c) gives a very different freezing pattern, with only a few small bubbles and no visible areas of concentrated solute. While mathematical smoothing has likely eliminated some of the smaller structures, the overall sample morphology is quite different than that produced by the same concentration of CsCl. Miedaner and Miedaner and co-workers (Miedaner, 2007; Miedaner et al., 2007), using different compounds, also found that sample morphology was highly sensitive to solute identity. Interestingly, changing solute in our system alters not only the structure of solute inclusions but also the size of the air bubbles. The exact reason for the change in morphology is unclear. CsCl is more polar than rose bengal and could influence the movement of the polar water molecules into the forming ice matrix. As a relatively large organic molecule, rose bengal might potentially modify the ice matrix due to its size. Finally, we note the thermodynamically predicted final concentration of solute ions at $-10\,^{\circ}C$ is 5.4 M; at this concentration CsCl should still be in solution, while a substantial portion of the rose bengal should have precipitated. Whether precipitated rose bengal is present as solids incorporated into the ice matrix or as precipitates in LLRs is not known.

The reproducibility of samples prepared on different days but using identical methods was quite good, with similar patterns seen for each replicate (Supplement Fig. S10). Each combination of the freezing method and solute gave a distinct distribution of solute and air bubbles, suggesting these two variables have a significant impact on ice morphology in our experimental system.

Table 1 lists the calculated volume of each material domain and the total CsCl mass present, including all sample voxels, based on segmentation described in the Methods section. As seen in the images and histogram, the freezer sample has the highest fraction (0.00019) of voxels containing 10 % or more LLR volume, approximately 5 times greater than the freeze chamber sample. In contrast, the fraction of voxels with $V_{LLR}/V_{VOXEL} = 2$–$10\,\%$ in the freezer sample (0.003) is about half that in the freeze chamber sample, and the frac-

tion of gas bubbles appears to be less than in the freeze chamber sample. However, this may be a computational artifact; voxels containing LLR next to gas bubbles will have a grayscale value somewhere between air and LLR, and therefore may be mistakenly counted as water ice voxels. Unfortunately, determining the magnitude of this error is difficult – requiring estimating the surface area of both air bubbles and any adjacent LLRs to identify suspect voxels – and is beyond the scope of this study. Because LLRs in the freezer samples are more concentrated and appear to be more frequently found next to air bubbles (as seen in Fig. 3b), this effect may be more pronounced in the freezer samples than freeze chamber samples. However, the number of voxels mistakenly classified as water (or less concentrated solute) is limited to boundaries between air and LLRs and therefore small, and it should not affect the overall interpretation of results. When the location of the CsCl mass is examined, more than 10 % of all CsCl present in the freezer sample is found in voxels with LLRs > 10 %, while in the freeze chamber sample only around 1 % of the mass is found in these most concentrated LLRs. For both freezer and freeze chamber samples, about two-thirds of the CsCl mass is found in the ice compartment, suggesting most solutes are present in very small LLR inclusions that are indistinguishable from water ice. For the LN2 sample, only 12 % of the mass is found in detectable LLRs, with the remainder distributed throughout the water ice. It is also possible that the CsCl in the LN2 samples is present not as liquid inclusions but as solid solution within the water ice. However, the solubility of HCl in solid ice is $(1–2) \times 10^{-4}$ M (Gross et al., 1975), while the CsCl solubility in solid ice would need to be 5–10 times greater, assuming all the CsCl is present in solid solution. The "missing" CsCl mass here is $0.88 \times 126.3\,\mu g = 111.1\,\mu g$, or 0.66 µmol. Assuming this solute is entirely present as LLRs with solute concentration of 2.7 M, this equates to a total LLR volume of 0.24 µL. The volume of pure ice (again from Table 1) is 725 µL. Therefore, assuming the remaining CsCl is distributed equally throughout the voxels labeled as pure ice in Table 1, the calculated average V_{LLR}/V_{VOXEL} for these voxels is 0.034 %, indistinguishable from water ice in our system. While it is possible the CsCl is present (at least partially) as solutes in the solid ice matrix, we believe it is more likely to be present primarily as small LLR inclusions. Additionally, we present evidence later in this paper supporting the idea that solutes are predominantly present as LLR inclusions.

We next examined the impact of sample container on sample morphology and solute distribution by imaging samples frozen in plastic vials instead of the glass vials we used above. While many of the samples discussed thus far were frozen in the laboratory freezer, most of the samples prepared in plastic vials were frozen in the freeze chamber. Therefore, to allow appropriate comparisons, we first present a sample of water (no solute) frozen in the freeze chamber and compare this with previous samples frozen in the freezer. Milli-Q water frozen in the freeze chamber in a glass vial (Supplement Fig. S11) gives similar spatial distribution to and somewhat smaller air bubble sizes than a similar sample frozen in a laboratory freezer (Fig. 2a and Supplement Fig. S1). However, freezing water in a plastic vial rather than glass can make a significant difference in ice morphology, as shown in Supplement Fig. S12. While ice in a glass vial forms many roughly spherical bubbles, water frozen in a plastic vial using our freeze chamber forms long vertical channels; such directional growth of air bubbles in a freezing liquid has previously been reported (Carte, 1961). While the reason for this morphology is not entirely clear, we believe it is related to how heat is removed from the sample during freezing. Because plastic conducts heat more poorly than water, ice, or glass, the vial walls act as insulators, forcing heat to be primarily removed from the bottom of the sample where the plastic vial contacts the chilled plate at the base of the freeze chamber. This may promote the formation of vertical air channels as the ice freezes upwards through the sample, rather than from the walls towards the interior in the glass vial sample.

We next examine the impact of freezing in plastic for a sample containing solutes. Supplement Fig. S13 shows a 1.0 mM CsCl solution frozen in the freezer in a plastic vial; compared to the similarly treated sample frozen in a glass vial (Fig. 3a), the air bubbles and concentrated inclusions are smaller in the plastic vial. Interestingly, the air bubbles in the plastic vial CsCl freezer sample do not show any of the elongation found when Milli-Q water is frozen in a plastic vial in the freeze chamber (Supplement Fig. S12), which may be related to the directional heat removal in the freeze chamber. Finally, once again using the freeze chamber, Supplement Fig. S14 shows 1.0 mM rose bengal frozen in plastic in the freeze chamber. Here, we see substantial volumes of LLRs and more bubbles than seen in the sample frozen in a glass vial, but without any elongation to bubbles or LLRs.

We also performed several other experiments to examine the nature of LLRs. Figure 4 shows a cross section of microCT images of the same sample (1.0 mM CsCl, frozen in freezer) at voxel resolutions of 16 (left) and 2 µm (right); the corresponding movies are in Supplement Fig. S15. The areas of light gray in the lower-resolution image (16 µm voxel resolution), such as the area highlighted by the arrow, are likely areas where CsCl is present in small areas of concentrated LLRs bordered by pure water ice, although the voxel resolution does not show these features separately. As would be expected if freezing water effectively excludes solutes from the forming bulk ice matrix, the right-hand image shows areas of concentrated LLRs adjacent to areas of pure water ice, supporting the idea discussed earlier that during freezing solutes are preferentially excluded from the forming ice matrix into small areas of concentrated solution. The higher-resolution image in Fig. 4 also shows very clearly how the solutes in LLRs often wrap around the bubbles in the freezer CsCl samples.

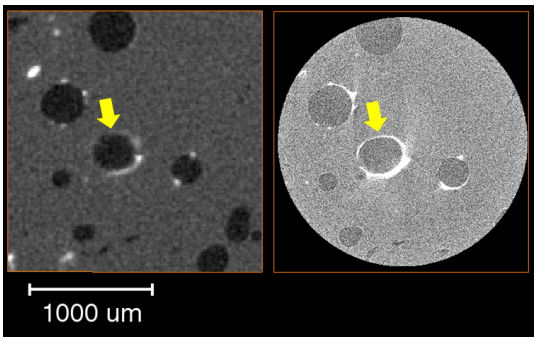

Figure 4. Side-by-side microCT cross sections of the same sample (1.0 mM CsCl, frozen in laboratory freezer) imaged at approximately 16 µm **(a)** and 2 µm **(b)** voxel sizes. Lighter tones indicate areas of higher radiodensity, i.e., higher solute amounts. The scale bar applies to both images.

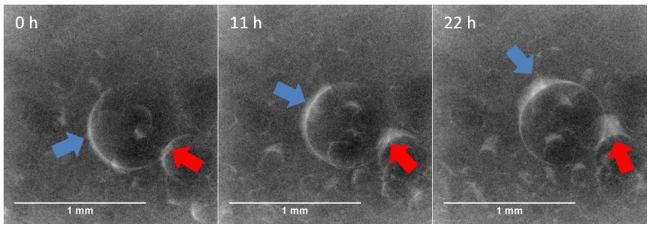

Figure 5. Vertically sliced X-ray images of a 1.0 mM CsCl ice (laboratory freezer, voxel resolution ∼ 2 µm) after 0, 11, and 22 h in the CT sample chamber. Lighter tones indicate areas of higher radiodensity (e.g., greater CsCl amounts). Air bubbles are visible as darker gray spheres. The temperature of the sample holder was set at −10 °C, but the top of the sample was approximately 1.3 °C warmer than the bottom, corresponding to a temperature gradient of approximately 0.13 °C mm^{-1}. Arrows highlight two of the areas where CsCl moves along the direction of the temperature gradient, from colder to warmer.

Finally, Fig. 5 (and the accompanying movie in Supplement Fig. S16) further supports the idea that CsCl is contained in liquid-like regions in our ice samples. We placed a 1.0 mM CsCl sample (glass vial; freezer) in the microCT sample holder set at −10 °C and took images of the sample (2 µm voxel resolution, x–z plane) at 0, 11, and 22 h. The temperature gradient in the sample holder was measured later by placing a thermocouple sensor between the glass vial and the holder wall at various positions. The temperature difference between the bottom and middle of the holder (approximately 1.7 cm, extending above and below the 1 cm height of the frozen sample in the vial) was 2.2 °C, resulting in a temperature gradient of 0.13 °C mm^{-1}. As seen in the three images, over the 22 h of this experiment the bright areas of CsCl move in the direction of the temperature gradient, towards the warmer top of the vial, at a rate of approximately 10 µm h^{-1} (i.e., 7.7 µm h^{-1}/(K^{-1} cm^{-1})). In many cases, the solutes appear to be migrating around the surfaces of air bubbles, which are visible as darker gray spheres. While the air bubbles appear to remain stationary in the ice matrix, with an estimated maximum migration rate of 0.15 µm h^{-1}/(K^{-1} cm^{-1}), the CsCl moves. Solutes are excluded from the forming ice matrix during freezing (Hobbs, 1974; Petrenko and Whitworth, 1999); here, it appears the solutes are present as a concentrated liquid-like solution, which can migrate either along the boundaries between air bubbles and the bulk ice or possibly by melting into the bulk ice itself (Notz and Worster, 2009). While we cannot rule out the possibility that the migrating solutes might be present as solid salt crystals, as seen in other work for ice under a temperature gradient (Light et al., 2009), the moving solutes in our images appear to be in liquid-like regions. Previous studies have found bubbles migrate in a temperature gradient at rates of around 1.5–3 µm h^{-1}/(K^{-1} cm^{-1}) (Dadic et al., 2010), while brine inclusions move at around 10 µm h^{-1}/(K^{-1} cm^{-1}) (Light et al., 2009). While our results support the idea of brine moving faster than bubbles, the relative rates in our experiments seem much different (with the bubbles moving slower and the brine moving faster) than suggested by previous literature. However, the earlier studies were done in systems containing either bubbles or brine inclusions, not both; as noted by Light et al. (2009), "The effect of included gas bubbles on brine migration has not been studied."

4 Implications and conclusions

Using microCT, we directly visualized the locations of solute, gas, and bulk ice in laboratory-prepared ice samples. While the chemical concentrations we used are higher than those in clean polar samples, because of the substantial morphological differences seen between pure ice samples and solute-containing samples, we expect that solutes in natural snow and ice might sometimes have important impacts on sample morphology, including the location and sizes of liquid-like regions and air bubbles.

Highlighting the sensitivity of ice structure to freezing conditions, we found a large difference between samples prepared at freezing temperatures in an upright freezer (where the sample was surrounded by cold air) vs. our custom-built freeze chamber (where the sample sat on a cold plate). Samples frozen in liquid nitrogen, as expected, did not have the large air bubbles and LLR inclusions found in freezer or freeze chamber samples; nonetheless, we did find some evidence for the segregation of solutes into LLRs, even with the fast freezing of liquid nitrogen.

In addition to freezing conditions, the choice of solute (either cesium chloride or rose bengal) also impacted the ice sample structure differently; CsCl yielded larger air bubbles and solute inclusions compared to rose bengal. While the observed variations in the locations and sizes of solute inclusions might be expected for solutes of different polarity and size, the influence of solute on bubble morphology

is more surprising. CsCl samples frozen in our laboratory freezer showed large LLRs, often wrapping around air bubbles. While QLLs at the surface ice–air interface of ice or snow are obviously in contact with atmospheric oxidants, the preferential collocation of internal LLRs and air bubbles represents a previously unrecognized air–ice interface. Depending on the chemistry occurring at this interface, the bubbles might be a source of oxidants and other gas-phase chemicals to internal solutes, and they might have significant impacts for chemical transformations under certain conditions.

Our results here suggest that subtle changes in the preparation of laboratory ice samples can have significant impacts on the location of solutes in samples, requiring careful and consistent sample preparation to ensure meaningful results. Ideally, researchers would directly evaluate the location of solutes for each sample preparation method, as we have done here; we recognize, however, this is a significant undertaking and not possible for every laboratory to do. Beyond the impacts on laboratory science, our work here may be able to help guide further investigations to understand the driving forces shaping snow and ice structures in the natural world, as well as investigations of the rate of chemical reactions in various compartments in snow and ice.

5 Data availability

The authors are happy to provide underlying datasets on request.

Information about the Supplement

Supplemental information is available at doi:10.1594/PANGAEA.855461. Captions for the Supplement figures can be found in the Supplement for this article.

The Supplement related to this article is available online at doi:10.5194/tc-10-2057-2016-supplement.

Acknowledgements. We gratefully acknowledge thorough and insightful comments from Hans-Werner Jacobi, Sönke Maus, and one anonymous reviewer. We thank Doug Rowland for microCT imaging assistance, David Paige (Paige Instruments) for constructing the temperature-controlled microCT sample chamber, and Bill Simpson and Peter Peterson for useful conversations and suggestions. We are grateful for funding from the National Science Foundation (grants CHE-1214121 and 1204169).

Edited by: C. Haas
Reviewed by: H.-W. Jacobi, S. Maus, and one anonymous referee

References

Barnes, P. R. F., Wolff, E. W., Mallard, D. C., and Mader, H. M.: SEM studies of the morphology and chemistry of polar ice, Microsc. Res. Techniq., 62, 62–69, doi:10.1002/jemt.10385, 2003.

Barret, M., Domine, F., Houdier, S., Gallet, J. C., Weibring, P., Walega, J., Fried, A., and Richter, D.: Formaldehyde in the Alaskan Arctic snowpack: Partitioning and physical processes involved in air-snow exchanges, J. Geophys. Res.-Atmos., 116, D00R03, doi:10.1029/2011jd016038, 2011.

Bartels-Rausch, T., Jacobi, H.-W., Kahan, T. F., Thomas, J. L., Thomson, E. S., Abbatt, J. P. D., Ammann, M., Blackford, J. R., Bluhm, H., Boxe, C., Domine, F., Frey, M. M., Gladich, I., Guzmán, M. I., Heger, D., Huthwelker, Th., Klán, P., Kuhs, W. F., Kuo, M. H., Maus, S., Moussa, S. G., McNeill, V. F., Newberg, J. T., Pettersson, J. B. C., Roeselová, M., and Sodeau, J. R.: A review of air–ice chemical and physical interactions (AICI): liquids, quasi-liquids, and solids in snow, Atmos. Chem. Phys., 14, 1587–1633, doi:10.5194/acp-14-1587-2014, 2014.

Beine, H., Anastasio, C., Esposito, G., Patten, K., Wilkening, E., Domine, F., Voisin, D., Barret, M., Houdier, S., and Hall, S.: Soluble, light-absorbing species in snow at Barrow, Alaska, J. Geophys. Res.-Atmos., 116, D00R05, doi:10.1029/2011jd016181, 2011.

Beine, H. J., Domine, F., Simpson, W., Honrath, R. E., Sparapani, R., Zhou, X. L., and King, M.: Snow-pile and chamber experiments during the Polar Sunrise Experiment "Alert 2000": exploration of nitrogen chemistry, Atmos. Environ., 36, 2707–2719, doi:10.1016/s1352-2310(02)00120-6, 2002.

Blanke, A., Beckmann, F., and Misof, B.: The head anatomy of Epiophlebia superstes (Odonata: Epiophlebiidae), Org. Divers. Evol., 13, 55–66, doi:10.1007/s13127-012-0097-z, 2013.

Carte, A. E.: Air bubbles in ice, P. Phys. Soc. Lond., 77, 757–768, doi:10.1088/0370-1328/77/3/327, 1961.

Chen, S. and Baker, I.: Evolution of individual snowflakes during metamorphism, J. Geophys. Res.-Atmos., 115, D21114, doi:10.1029/2010jd014132, 2010.

Cheng, J., Soetjipto, C., Hoffmann, M. R., and Colussi, A. J.: Confocal Fluorescence Microscopy of the Morphology and Composition of Interstitial Fluids in Freezing Electrolyte Solutions, J. Phys. Chem. Lett., 1, 374–378, doi:10.1021/jz9000888, 2010.

Cho, H., Shepson, P. B., Barrie, L. A., Cowin, J. P., and Zaveri, R.: NMR investigation of the quasi-brine layer in ice/brine mixtures, J. Phys. Chem. B, 106, 11226–11232, doi:10.1021/jp020449+, 2002.

Chu, L. and Anastasio, C.: Quantum yields of hydroxyl radical and nitrogen dioxide from the photolysis of nitrate on ice, J. Phys. Chem. A, 107, 9594–9602, doi:10.1021/jp0349132, 2003.

Chu, L. and Anastasio, C.: Formation of hydroxyl radical from the photolysis of frozen hydrogen peroxide, J. Phys. Chem. A, 109, 6264–6271, doi:10.1021/jp051415f, 2005.

Dadic, R., Light, B., and Warren, S. G.: Migration of air bubbles in ice under a temperature gradient, with application to "Snowball Earth", J. Geophys. Res.-Atmos., 115, D18125, doi:10.1029/2010jd014148, 2010.

Dibb, J. E. and Arsenault, M.: Shouldn't snowpacks be sources of monocarboxylic acids?, Atmos. Environ., 36, 2513–2522, 2002.

Domine, F. and Shepson, P. B.: Air-snow interactions and atmospheric chemistry, Science, 297, 1506–1510, 2002.

Domine, F., Albert, M., Huthwelker, T., Jacobi, H.-W., Kokhanovsky, A. A., Lehning, M., Picard, G., and Simpson, W. R.: Snow physics as relevant to snow photochemistry, Atmos. Chem. Phys., 8, 171–208, doi:10.5194/acp-8-171-2008, 2008.

Douglas, T. A. and Sturm, M.: Arctic haze, mercury and the chemical composition of snow across northwestern Alaska, Atmos. Environ., 38, 805–820, doi:10.1016/j.atmosenv.2003.10.042, 2004.

Evans, N. J., McInnes, B. I. A., Squelch, A. P., Austin, P. J., McDonald, B. J., and Wu, Q. H.: Application of X-ray micro-computed tomography in (U-Th)/He thermochronology, Chem. Geol., 257, 101–113, doi:10.1016/j.chemgeo.2008.08.021, 2008.

Grannas, A. M., Jones, A. E., Dibb, J., Ammann, M., Anastasio, C., Beine, H. J., Bergin, M., Bottenheim, J., Boxe, C. S., Carver, G., Chen, G., Crawford, J. H., Dominé, F., Frey, M. M., Guzmán, M. I., Heard, D. E., Helmig, D., Hoffmann, M. R., Honrath, R. E., Huey, L. G., Hutterli, M., Jacobi, H. W., Klán, P., Lefer, B., McConnell, J., Plane, J., Sander, R., Savarino, J., Shepson, P. B., Simpson, W. R., Sodeau, J. R., von Glasow, R., Weller, R., Wolff, E. W., and Zhu, T.: An overview of snow photochemistry: evidence, mechanisms and impacts, Atmos. Chem. Phys., 7, 4329–4373, doi:10.5194/acp-7-4329-2007, 2007.

Gross, G. W., Wu, C. H., Bryant, L., and McKee, C.: Concentration dependent solute redistribution at ice-water phase boundary. 2. Experimental investigation, J. Chem. Phys., 62, 3085–3092, doi:10.1063/1.430909, 1975.

Hallett, J.: Experimental studies of the crystallization of supercooled water, J. Atmos. Sci., 21, 671–682, doi:10.1175/1520-0469(1964)021<0671:esotco>2.0.co;2, 1964.

Haynes, W. M. E.: CRC Handbook of Chemistry and Physics, 95 ed., CRC Press, Boca Raton, Florida, USA, 2014.

Heger, D., Jirkovsky, J., and Klan, P.: Aggregation of methylene blue in frozen aqueous solutions studied by absorption spectroscopy, J. Phys. Chem. A, 109, 6702–6709, doi:10.1021/jp050439j, 2005.

Heger, D., Klanova, J., and Klan, P.: Enhanced protonation of cresol red in acidic aqueous solutions caused by freezing, J. Phys. Chem. B, 110, 1277–1287, doi:10.1021/jp0553683, 2006.

Heggli, M., Kochle, B., Matzl, M., Pinzer, B. R., Riche, F., Steiner, S., Steinfeld, D., and Schneebeli, M.: Measuring snow in 3-D using X-ray tomography: assessment of visualization techniques, Ann. Glaciol., 52, 231–236, 2011.

Hobbs, P. V.: Ice Physics, Oxford University Press, Oxford, England, 1974.

Hullar, T. and Anastasio, C.: Yields of hydrogen peroxide from the reaction of hydroxyl radical with organic compounds in solution and ice, Atmos. Chem. Phys., 11, 7209–7222, doi:10.5194/acp-11-7209-2011, 2011.

Hullar, T., Paige, D. F., Rowland, D. J., and Anastasio, C.: Compact cold stage for micro-computerized tomography imaging of chilled or frozen samples, Rev. Sci. Instrum., 85, 043708, doi:10.1063/1.4871473, 2014.

Jacobi, H. W., Bales, R. C., Honrath, R. E., Peterson, M. C., Dibb, J. E., Swanson, A. L., and Albert, M. R.: Reactive trace gases measured in the interstitial air of surface snow at Summit, Greenland, Atmos. Environ., 38, 1687–1697, doi:10.1016/j.atmosenv.2004.01.004, 2004.

Jacobi, H. W., Annor, T., and Quansah, E.: Investigation of the photochemical decomposition of nitrate, hydrogen peroxide, and formaldehyde in artificial snow, J. Photoch. Photobio. A, 179, 330–338, doi:10.1016/j.jphotochem.2005.09.001, 2006.

Kahan, T. F. and Donaldson, D. J.: Photolysis of polycyclic aromatic hydrocarbons on water and ice surfaces, J. Phys. Chem. A, 111, 1277–1285, doi:10.1021/jp066660t, 2007.

Kahan, T. F. and Donaldson, D. J.: Benzene photolysis on ice: Implications for the fate of organic contaminants in the winter, Environ. Sci. Technol., 44, 3819–3824, doi:10.1021/es100448h, 2010.

Kahan, T. F., Zhao, R., Jumaa, K. B., and Donaldson, D. J.: Anthracene photolysis in aqueous solution and ice: Photon flux dependence and comparison of kinetics in bulk ice and at the air-ice interface, Environ. Sci. Technol., 44, 1302–1306, doi:10.1021/es9031612, 2010.

Kurkova, R., Ray, D., Nachtigallova, D., and Klan, P.: Chemistry of small organic molecules on snow grains: The applicability of artificial snow for environmental studies, Environ. Sci. Technol., 45, 3430–3436, doi:10.1021/es104095g, 2011.

Lake, R. A. and Lewis, E. L.: Salt rejection by sea ice during growth, J. Geophys. Res., 75, 583–597, doi:10.1029/JC075i003p00583, 1970.

Light, B., Brandt, R. E., and Warren, S. G.: Hydrohalite in cold sea ice: Laboratory observations of single crystals, surface accumulations, and migration rates under a temperature gradient, with application to "Snowball Earth", J. Geophys. Res.-Oceans, 114, C07018, doi:10.1029/2008jc005211, 2009.

Lomonaco, R., Albert, M., and Baker, I.: Microstructural evolution of fine-grained layers through the firn column at Summit, Greenland, J. Glaciol., 57, 755–762, 2011.

Lomonaco, R. W., Chen, S., and Baker, I.: Characterization of porous snow with SEM and Micro CT, Microsc. Microanal., 15, 1110–1111, doi:10.1017/s1431927609093313, 2009.

McFall, A. S. and Anastasio, C.: Photon flux dependence on solute environment in water ices, Environ. Chem., 13, 682–687, doi:10.1071/EN15199, 2016.

Miedaner, M.: Characterization of inclusions and their distribution in natural and artificial ice samples by synchrotron cryo-micro-tomography (SCXRTM), thesis, Johannes Gutenberg Universität, Mainz, Germany, 2007.

Miedaner, M. M., Huthwelker, T., Enzmann, F., Kersten, M., Stampanoni, M., and Ammann, M.: X-ray tomographic characterization of impurities in polycrystalline ice, Physics and Chemistry of Ice, edited by: Kuhs, W. F., Royal Society of Chemistry, Cambridge, UK, 399–407, 2007.

Neckers, D. C.: Rose Bengal, J. Photoch. Photobio. A, 47, 1–29, doi:10.1016/1010-6030(89)85002-6, 1989.

NIST: X-ray form factor, attenuation, and scattering tables, available at: http://physics.nist.gov/PhysRefData/FFast/html/form.html, last access: 5 July 2015.

Notz, D. and Worster, M. G.: Desalination processes of sea ice revisited, J. Geophys. Res.-Oceans, 114, C05006, doi:10.1029/2008jc004885, 2009.

NIH: PubChem Open Chemistry Database, available at: http://pubchem.ncbi.nlm.nih.gov, last access: 7 July 2015.

Obbard, R. W., Troderman, G., and Baker, I.: Imaging brine and air inclusions in sea ice using micro-X-ray computed tomography, J. Glaciol., 55, 1113–1115, 2009.

Petrenko, V. F. and Whitworth, R. W.: Physics of Ice, Oxford University Press, Oxford, England, 1999.

Phillips, G. J. and Simpson, W. R.: Verification of snowpack radiation transfer models using actinometry, J. Geophys. Res.-Atmos., 110, D08306 doi:10.1029/2004jd005552, 2005.

Pruppacher, H. R. and Klett, J. D.: Microphysics of clouds and precipitation, Vol. 18 of Atmospheric and oceanographic sciences library, Kluwer Acadamics Publ., Dordrecht, the Netherlands, 2010.

Ram, K. and Anastasio, C.: Photochemistry of phenanthrene, pyrene, and fluoranthene in ice and snow, Atmos. Environ., 43, 2252–2259, doi:10.1016/j.atmosenv.2009.01.044, 2009.

Rohatgi, P. and Adams, C.: Ice-brine dendritic aggregate formed on freezing of aqueous solutions, J. Glaciol., 6, 663–679, 1967.

Rosenthal, W., Saleta, J., and Dozier, J.: Scanning electron microscopy of impurity structures in snow, Cold Reg. Sci. Technol., 47, 80–89, doi:10.1016/j.coldregions.2006.08.006, 2007.

Shumskii, P. A.: Principles of Structural Glaciology, Dover Publications, Inc., New York, USA, 1964.

Sumner, A. L. and Shepson, P. B.: Snowpack production of formaldehyde and its effect on the Arctic troposphere, Nature, 398, 230–233, 1999.

Wettlaufer, J. S., Worster, M. G., and Huppert, H. E.: Natural convection during solidification of an alloy from above with application to the evolution of sea ice, J. Fluid Mech., 344, 291–316, doi:10.1017/s0022112097006022, 1997.

Yang, Q., Mayewski, P. A., Linder, E., Whitlow, S., and Twickler, M.: Chemical species spatial distribution and relationship to elevation and snow accumulation rate over the Greenland Ice Sheet, J. Geophys. Res.-Atmos., 101, 18629–18637, doi:10.1029/96jd01061, 1996.